Similarity solution of temperature structure functions in decaying homogeneous isotropic turbulence

R. A. Antonia,[1] R. J. Smalley,[2] T. Zhou,[3] F. Anselmet,[4] and L. Danaila[5]
[1]*Discipline of Mechanical Engineering, University of Newcastle, New South Wales 2308, Australia*
[2]*Energy and Resources Research Institute, University of Leeds, Leeds LS2 9JT, United Kingdom*
[3]*School of Mechanical & Production Engineering, Nanyang Technological University, Singapore 639798, Singapore*
[4]*IRPHE, Université d'Aix-Marseille I & II, 13384 Marseille, France*
[5]*CORIA, Avenue de l'Université, Boîte Postale 12, 76801 St. Etienne du Rouvray, France*
(Received 16 June 2003; published 26 January 2004)

An equilibrium similarity analysis is applied to the transport equation for $\langle(\delta\theta)^2\rangle$, the second-order temperature structure function, for decaying homogeneous isotropic turbulence. A possible solution is that the temperature variance $\langle\theta^2\rangle$ decays as x^n, and that the characteristic length scale, identifiable with the Taylor microscale λ, or equivalently the Corrsin microscale λ_θ, varies as $x^{1/2}$. The turbulent Reynolds and Péclet numbers decay as $x^{(m+1)/2}$ when $m<-1$, where m is the exponent which characterizes the decay of the turbulent energy $\langle q^2\rangle$, viz., $\langle q^2\rangle\sim x^m$. Measurements downstream of a grid-heated mandoline combination show that, like $\langle(\delta q)^2\rangle$, $\langle(\delta\theta)^2\rangle$ satisfies similarity approximately over a significant range of scales r, when λ, λ_θ, $\langle q^2\rangle$, and $\langle\theta^2\rangle$ are used as the normalizing scales. This approximate similarity is exploited to calculate the third-order structure functions. Satisfactory agreement is found between measured and calculated distributions of $\langle\delta u(\delta q)^2\rangle$ and $\langle\delta u(\delta\theta)^2\rangle$, where δu is the longitudinal velocity increment.

DOI: 10.1103/PhysRevE.69.016305 PACS number(s): 47.27.Te

I. INTRODUCTION

Since the earlier seminal work of Corrsin [1], much effort has been devoted to studying the decay of temperature fluctuations in isotropic turbulence. In particular, there have been numerous experimental attempts to investigate the decay of temperature fluctuations introduced in grid-generated turbulence. Perhaps a major outcome of these studies is the observation that the decay rate of the scalar (as well as the shape of the scalar spectrum) is more significantly affected by initial conditions than the corresponding velocity characteristics (e.g., Warhaft and Lumley [2], Sreenivasan *et al.* [3]).

An analytical description of the decay of velocity and scalar fluctuations in isotropic turbulence was considerably facilitated by the hypothesis of self-preservation or similarity, initially applied to the equation for two-point velocity correlations (Karman and Howarth [4]) (see Antonia *et al.* [5], hereafter referred to as I, for a brief review of previous results pertaining to the similarity of the velocity field) and later extended to two-point temperature correlations [1]. Although the consequences of similarity have been investigated widely, grid turbulence data have not provided a fully satisfactory verification of the hypothesis (e.g., Monin and Yaglom [6]). The analyses of George [7] and Speziale and Bernard [8] both dealt with the velocity field but the approaches differed in significant ways. George [7] analyzed the spectral energy equation

$$\frac{\partial E(k)}{\partial t}=T(k)-2\nu k^2E(k), \tag{1}$$

where $E(k)$ is the three-dimensional (3D) energy spectrum, k is the magnitude of the wave number $\tilde{k}$, and $T(k)$ is the non-linear spectral transfer function. It was found that Eq. (1) admitted equilibrium similarity, irrespective of the magnitude of the Reynolds number. The energy $\langle q^2\rangle$ decayed according to a power law, viz. $\langle q^2\rangle\sim t^m$ $(m<-1)$, the exponent m depending on initial conditions.

Speziale and Bernard [8] carried out a fixed point analysis on an equation which combines the transport equation for two-point velocity correlations $\langle u(x)u(x+r)\rangle$ with the transport equation for $\langle\epsilon\rangle$, the mean energy dissipation rate. Two possible similarity solutions were found, one with $\langle q^2\rangle\sim t^{-1}$ (at very high Reynolds numbers) and the other with $\langle q^2\rangle\sim t^m$ $(m>-1)$ achieved in the limit of vanishing turbulence Reynolds number. These authors assumed in essence that the velocity derivative skewness $S\equiv-\langle(\partial u/\partial x)^3\rangle/\langle(\partial u/\partial x)^2\rangle^{3/2}$ remained constant during decay and inferred that R_λ should be constant. This follows immediately from George [7], who says only that the product SR_λ is constant with no further assumption about either S or R_λ. For both George [7] and Speziale and Bernard, the relevant velocity scale was $\langle q^2\rangle^{1/2}$ and, the relevant length scale was λ, the Taylor microscale.

George [9] examined the conditions under which the scalar spectral equation

$$\frac{\partial}{\partial t}E_\theta(k)=T_\theta(k)-2\kappa k^2E_\theta(k) \tag{2}$$

satisfies similarity (this will be defined more precisely in Sec. II). In Eq. (2), $E_\theta(k)$ is the 3D scalar spectrum, $T_\theta(k)$ is the spectral scalar transfer function, κ is the thermal diffusivity of the fluid. George [9] found that a complete similarity solution was possible when the temperature variance

$$\langle\theta^2\rangle=\int_0^\infty E_\theta(k)dk \tag{3}$$

varied according to a power-law behavior, viz. $\langle\theta^2\rangle \sim t^n$, and the length scale, which was readily identifiable with Corrsin's microscale λ_θ, increased as $t^{1/2}$. The decay exponent n and the spectral shape are determined by the initial conditions. Gonzalez and Fall [10] extended the approach of Ref. [8] to analyze the self-preserving decay of scalar fluctuations in isotropic turbulence. They found that self-preservation was possible for the same two asymptotic states which were identified for the velocity field. In particular, for very large Reynolds and Péclet numbers, the power-law exponent of $\langle\theta^2\rangle$ was found to depend on the velocity derivative skewness S, the mixed velocity-temperature derivative skewness $S_\theta \equiv -\langle(\partial u/\partial x)(\partial\theta/\partial x)^2\rangle/\langle(\partial u/\partial x)^2\rangle^{1/2}\langle(\partial\theta/\partial x)^2\rangle$, $G \equiv \langle u^2\rangle\langle(\partial^2 u/\partial x^2)^2\rangle/\langle(\partial u/\partial x)^2\rangle^2$, or destruction coefficient of enstrophy and $G_\theta \equiv \langle\theta^2\rangle\langle(\partial^2\theta/\partial x^2)^2\rangle/\langle(\partial\theta/\partial x)^2\rangle^2$ or destruction coefficient of scalar enstrophy. The dependence on t is replaced by a dependence on x, to facilitate comparison with experimental results. The parameters S, S_θ, G, G_θ remained constant during decay. A consequence of George [7] and George [9] is that G, G_θ as well as the products SR_λ and $S_\theta R_\lambda$ should remain constant during decay.

The velocity spectra measured by Comte-Bellot and Corrsin [11] satisfied George [7] to a good approximation. Except at the lowest wave numbers, the temperature spectra of Warhaft and Lumley [2] also supported George [9] reasonably well.

While direct numerical simulations (DNS) are useful for assessing different similarity hypotheses and their consequences [12], it is equally important to use experiments for testing proposals such as George [7] or George [9]. Certainly, DNS and experiment complement each other (each approach has advantages and shortcomings). In particular, the structure function approach, which is adopted here, lends itself better to measurements [since $E_\theta(k)$ and $T_\theta(k)$ are not directly measurable]. The focus in DNS is usually spectral.

In I, it was shown that, for decaying isotropic turbulence, the transport equation for $\langle(\delta q)^2\rangle \equiv \langle(\delta u)^2\rangle + \langle(\delta v)^2\rangle + \langle(\delta w)^2\rangle$ [$\delta\alpha \equiv \alpha(x+r) - \alpha(x)$, $\alpha \equiv u$, v, w, the velocity fluctuations in the x, y, z directions, respectively, and r is the streamwise separation between the two points], viz.,

$$-\langle(\delta u)(\delta q)^2\rangle + 2\nu\frac{d}{dr}\langle(\delta q)^2\rangle - \frac{U}{r^2}\int_0^r s^2\frac{\partial}{\partial x}\langle(\delta q)^2\rangle ds = \frac{4}{3}\langle\epsilon\rangle r \tag{4}$$

admitted a similarity solution, with $\langle q^2\rangle \sim x^m$ and $\lambda \sim x^{1/2}$. U is the mean streamwise velocity, $\langle\epsilon\rangle$ is the mean kinetic energy dissipation rate, and s is a dummy separation variable. Note that Eq. (4) is the more general form of the equation for $\langle(\delta u)^3\rangle$:

$$-\langle(\delta u)^3\rangle + 6\nu\frac{d}{dr}\langle(\delta u)^2\rangle - 3\frac{U}{r^4}\int_0^r s^4\frac{\partial}{\partial x}\langle(\delta u)^2\rangle ds = \frac{4}{5}\langle\epsilon\rangle r, \tag{5}$$

and corresponds fully to Eq. (1).

In the present paper, we consider (Sec. II) the conditions for which the transport equation for $\langle(\delta\theta)^2\rangle$ (Danaila *et al.* 1999, [13]), i.e.,

$$-\langle(\delta u)(\delta\theta)^2\rangle + 2\kappa\frac{d}{dr}\langle(\delta\theta)^2\rangle - \frac{U}{r^2}\int_0^r s^2\frac{\partial}{\partial x}\langle(\delta\theta)^2\rangle ds = \frac{4}{3}\langle\chi\rangle r, \tag{6}$$

conforms with similarity. In Eq. (6), $\langle\chi\rangle$ represents the mean dissipation rate of $\langle\theta^2\rangle/2$:

$$\langle\chi\rangle = 2\kappa\int_0^\infty k^2 E_\theta(k)dk. \tag{7}$$

A brief description of experimental conditions is given in Sec. III. The experimental data are assessed in Sec. IV in the context of the similarity requirements. An attraction of Eq. (6) is that, like the transport equation for $\langle(\delta q)^2\rangle$ [Eq. (4)], it is more amenable to experimental verification than Eqs. (1) or (2).

II. EQUILIBRIUM SIMILARITY OF TEMPERATURE STRUCTURE FUNCTION EQUATION

We consider the conditions under which Eq. (6) can satisfy similarity. It is assumed that

$$\langle(\delta\theta)^2\rangle = V_\theta f_\theta\left(\frac{r}{\mathcal{L}_\theta}\right) \tag{8}$$

and

$$-\langle(\delta u)(\delta\theta)^2\rangle = H_\theta g_\theta\left(\frac{r}{\mathcal{L}_\theta}\right), \tag{9}$$

where $\mathcal{L}_\theta$ (a characteristic length scale), V_θ (with dimensions of temperature squared), and H_θ (with dimensions of the product of velocity and temperature squared) fully characterize the streamwise decay of $\langle(\delta\theta)^2\rangle$ and $-\langle(\delta u)(\delta\theta)^2\rangle$. As in George [9], we avoid making the *a priori* assumption that H_θ is given by $V^{1/2}V_\theta$, where V has dimensions of velocity squared. The characteristic scales $\mathcal{L}_\theta$, V_θ, and H_θ depend on x only. The dimensionless functions f_θ and g_θ depend not only on $r/\mathcal{L}_\theta$ but also on the initial conditions of the flow, those at the mandoline where the scalar is introduced as well as those at the turbulence generating grid.

After substituting Eqs. (8) and (9) into Eq. (6), we obtain

$$H_\theta g_\theta + 2\kappa\frac{V_\theta}{\mathcal{L}_\theta}f'_\theta + UV_\theta\frac{d\mathcal{L}_\theta}{dx}\tilde{r}_\theta^{-2}\Gamma_{\theta_1} - U\mathcal{L}_\theta\frac{dV_\theta}{dx}\tilde{r}_\theta^{-2}\Gamma_{\theta_2} = -\frac{2}{3}U\mathcal{L}_\theta\frac{d\langle\theta^2\rangle}{dx}\tilde{r}_\theta, \tag{10}$$

where $\tilde{r}_\theta \equiv r/\mathcal{L}_\theta$ (a prime denotes differentiation with respect to $\tilde{r}_\theta$), $\Gamma_{\theta_1} = \int_0^{\tilde{r}_\theta}\tilde{s}_\theta^3 f'_\theta d\tilde{s}_\theta$, and $\Gamma_{\theta_2} = \int_0^{\tilde{r}_\theta}\tilde{s}_\theta^2 f_\theta d\tilde{s}_\theta$; s_θ is a

dummy separation variable. In Eq. (10), $\langle\chi\rangle$ was replaced by its corresponding value in decaying turbulence, viz.,

$$\langle\chi\rangle = -\frac{U}{2}\frac{d\langle\theta^2\rangle}{dx}. \tag{11}$$

After multiplication by $\mathcal{L}_\theta/\kappa V_\theta$, Eq. (10) becomes

$$\left[\frac{H_\theta\mathcal{L}_\theta}{\kappa V_\theta}\right]g_\theta + [2]f'_\theta + \left[\frac{U\mathcal{L}_\theta}{\kappa}\frac{d\mathcal{L}_\theta}{dx}\right]\tilde{r}_\theta^{-2}\Gamma_{\theta_1} - \left[\frac{U\mathcal{L}_\theta^2}{\kappa V_\theta}\frac{dV_\theta}{dx}\right]\tilde{r}_\theta^{-2}\Gamma_{\theta_2} = -\frac{2}{3}\left[\frac{U\mathcal{L}_\theta^2}{\kappa V_\theta}\frac{d\langle\theta^2\rangle}{dx}\right]\tilde{r}_\theta. \tag{12}$$

For equilibrium similarity, all the terms within square brackets should evolve in x in exactly the same way. Since one of them, the coefficient of f'_θ, is constant, the others must also be constant, viz.,

$$\frac{H_\theta\mathcal{L}_\theta}{\kappa V_\theta} = \text{const}, \tag{13}$$

$$\frac{U\mathcal{L}_\theta}{\kappa}\frac{d\mathcal{L}_\theta}{dx} = a_\theta, \tag{14}$$

$$\frac{U\mathcal{L}_\theta^2}{\kappa V_\theta}\frac{dV_\theta}{dx} = b_\theta, \tag{15}$$

$$\frac{U\mathcal{L}_\theta^2}{\kappa V_\theta}\frac{d\langle\theta^2\rangle}{dx} = \text{const}. \tag{16}$$

Integrating Eq. (14) with respect to x immediately yields

$$\mathcal{L}_\theta^2 = \frac{2\kappa}{U}a_\theta(x-x_0), \tag{17}$$

where $\mathcal{L}_\theta = 0$ at $x = x_0$. Comparison of Eqs. (15) and (16) suggests that the temperature variance can be taken as the appropriate characteristic scale for $\langle(\delta\theta)^2\rangle$, viz., $V_\theta \sim \langle\theta^2\rangle$. Integration of Eq. (15) or (16) suggests that a possible similarity solution of Eq. (6) is given by

$$\langle\theta^2\rangle = A_\theta(x-x_0)^n, \tag{18}$$

with $n \equiv b_\theta/2a_\theta$ and A_θ is a constant which may depend on initial conditions. A general definition of the Corrsin microscale λ_θ is given by

$$\lambda_\theta^2 = 3\kappa\frac{\langle\theta^2\rangle}{\langle\chi\rangle}. \tag{19}$$

This form of λ_θ reduces to the more conventional definition $\lambda_\theta^2 = \langle\theta^2\rangle/\langle(\partial\theta/\partial x)^2\rangle$ when isotropy is assumed, viz. $\langle\chi\rangle = 3\kappa\langle(\partial\theta/\partial x)^2\rangle$. After substituting $\langle\theta^2\rangle$ in Eq. (19), and using Eq. (11), we have

$$\lambda_\theta^2 = -\frac{6\kappa}{n}\frac{(x-x_0)}{U} \tag{20}$$

which is analogous to

$$\lambda^2 = -\frac{10\nu}{m}\frac{(x-x_0)}{U}. \tag{21}$$

Comparison of Eq. (20) with Eq. (17) suggests that $\mathcal{L}_\theta \equiv \lambda_\theta$ if $a_\theta = (-3/n)$. With $V_\theta \equiv \langle\theta^2\rangle$ and $\mathcal{L}_\theta \equiv \lambda_\theta$, Eq. (13) implies that $H_\theta \sim \kappa\langle\theta^2\rangle/\lambda_\theta$ or

$$H_\theta \sim \frac{\mathrm{Pe}^{-1}}{3^{1/2}}\langle q^2\rangle^{1/2}\langle\theta^2\rangle, \tag{22}$$

where Pe, the turbulent Péclet number, is defined by

$$\mathrm{Pe} = \frac{\langle q^2\rangle^{1/2}\lambda_\theta}{3^{1/2}\kappa}, \tag{23}$$

and is related to the turbulent Reynolds number R_λ by $\mathrm{Pe} = (3/5)^{1/2}R_\lambda \mathrm{Pr}^{1/2}R^{1/2}$, where

$$R_\lambda = \frac{\langle q^2\rangle^{1/2}}{3^{1/2}}\frac{\lambda}{\nu}, \tag{24}$$

Pr ($\equiv\nu/\kappa$) is the Prandtl number and

$$R = (\langle\theta^2\rangle/\langle\chi\rangle)/(\langle q^2\rangle/\langle\epsilon\rangle) \tag{25}$$

is the ratio between thermal and mechanical energy dissipation time scales. After some manipulation, Eq. (10) can be reduced to

$$g_\theta = 4\tilde{r}_\theta + \frac{3}{n}\tilde{r}_\theta^{-2}\Gamma_{\theta_1} - 6\tilde{r}_\theta^{-2}\Gamma_{\theta_2} - 2f'_\theta. \tag{26}$$

Equation (26) suggests that the normalized mixed third-order structure function g_θ can be uniquely determined once f_θ and n are known. The dependence of g_θ on initial conditions occurs implicitly through f_θ and n. In an experimental context, the initial conditions include, *inter alia*, the geometries of the grid and mandoline, the spacing between the grid and the mandoline, as well as the magnitude of R_M ($\equiv UM/\nu$), the Reynolds number at the grid (M is the grid mesh size).

The scalar integral length scale L_θ is defined by

$$L_\theta = \frac{\pi}{2\langle\theta^2\rangle}\int_0^\infty \frac{E_\theta(k)}{k}dk, \tag{27}$$

where $E_\theta(k)$ is the 3D scalar spectrum. Normalization by $\langle\theta^2\rangle$ and λ_θ yields

$$\frac{L_\theta}{\lambda_\theta} = \frac{\pi}{2}\int_0^\infty \frac{\tilde{E}_\theta(\tilde{k}_\theta)}{\tilde{k}_\theta}d\tilde{k}_\theta,$$

where $\tilde{k}_\theta \equiv k\lambda_\theta$ and $\tilde{E}_\theta(\tilde{k}_\theta) = \lambda_\theta E_\theta(k)/\langle\theta^2\rangle$ (in general, the tilde will denote normalization by λ or λ_θ and $\langle q^2\rangle$ or $\langle\theta^2\rangle$). Like $f_\theta(\tilde{r}_\theta)$, $\tilde{E}_\theta(\tilde{k}_\theta)$ cannot depend on x. It follows that L_θ/λ_θ remains constant with respect to x.

Another, more empirical measure of the scalar integral length scale is L_χ, defined as

$$L_\chi = C_\chi \frac{\langle \theta^2 \rangle}{\langle \chi \rangle} \frac{\langle q^2 \rangle^{1/2}}{3^{1/2}}. \tag{28}$$

The ratio L_χ/λ_θ may be written as

$$\frac{L_\chi}{\lambda_\theta} = \frac{C_\chi}{3} \mathrm{Pe}. \tag{29}$$

If C_χ is constant, constancy of L_χ/λ_θ requires that Pe does not vary with x.

When $\mathrm{Pr} \leqslant 1$ (the case of interest here), the smallest length scale may be identified with $\eta_\theta \equiv \kappa^{3/4}/\langle \epsilon \rangle^{1/4} = \eta \mathrm{Pr}^{-3/4}$ (when $\mathrm{Pr} > 1$, the smallest scale is the Batchelor length scale $\eta \mathrm{Pr}^{-1/2}$) and $\eta_\theta/\lambda_\theta$ may be written as

$$\frac{\eta_\theta}{\lambda_\theta} = \frac{\eta}{\lambda} \left(\frac{5}{3} \right)^{1/2} \mathrm{Pr}^{-1/4} R^{-1/2}. \tag{30}$$

Since $\eta/\lambda = 15^{-1/4} R_\lambda^{-1/2}$, $\eta_\theta/\lambda_\theta$ is constant only if R_λ is constant. Note that the constancy of R with x is guaranteed if $\langle q^2 \rangle$ and $\langle \theta^2 \rangle$ have power-law behaviors. It follows from the definition of R_λ and $\langle q^2 \rangle = A(x - x_0)^m$ (A is a constant which may depend on initial conditions; x_0 may differ from that for $\langle \theta^2 \rangle$) that R_λ and Pe are independent of x only if m is -1. For this case, which could *a priori* be expected to be attained at large R_λ and Pe, Kolmogorov similarity would be fully compatible with the present similarity solution. It should be underlined, however, that the latter does not require R_λ and Pe to be large, nor does it require them to remain constant with respect to x. While similarity of the velocity field is a necessary requisite for similarity of the scalar field, it is not sufficient. The magnitude of n is more constrained than that of m. These constraints can be identified from the transport equations for $\langle \epsilon \rangle$ and $\langle \chi \rangle$, which are the limiting forms of Eqs. (5) and (6) when $r \to 0$. For simplicity, only the isotropic forms of these equations are given below (e.g., Batchelor and Townsend [14], Zhou *et al.*, [15] hereafter II):

$$G = \frac{15}{7} \left(\frac{m-1}{m} \right) - \frac{S R_\lambda}{2}, \tag{31}$$

$$\frac{G_\theta}{R} = \frac{9}{10} \left(\frac{n-1}{m} \right) - \frac{9}{10} S_\theta R_\lambda. \tag{32}$$

While m depends on G, S, and R_λ, n also depends on G_θ and S_θ as well as on the previous parameters (through m).

It can be readily shown that similarity requires G and G_θ to remain constant since $G \sim \int_0^\infty \tilde{k}_1^4 \tilde{\phi}_u(\tilde{k}) d\tilde{k}_1 / [\int_0^\infty \tilde{k}_1^2 \tilde{\phi}_u(\tilde{k}_1) d\tilde{k}_1]^2$ and $G_\theta \sim \int_0^\infty \tilde{k}_1^4 \tilde{\phi}_\theta(\tilde{k}_1) d\tilde{k}_1 / [\int_0^\infty \tilde{k}_1^2 \tilde{\phi}_\theta(\tilde{k}_1) d\tilde{k}_1]$. It follows that the products SR_λ and $S_\theta R_\lambda$ must also remain constant.

Expression (26) for g_θ is analogous to that obtained in I for the normalized third-order velocity structure function, viz.,

$$g = \frac{20}{3} \tilde{r} + \frac{5}{m} \tilde{r}^{-2} \Gamma_1 - 10 \tilde{r}^{-2} \Gamma_2 - 2f', \tag{33}$$

where $g \equiv -3^{1/2} R_\lambda \langle (\delta \tilde{u})(\delta \tilde{q})^2 \rangle$, $\Gamma_1 = \int_0^{\tilde{r}} \tilde{s}^3 f' d\tilde{s}$, $\Gamma_2 = \int_0^{\tilde{r}} \tilde{s}^2 f d\tilde{s}$, and $f = \langle (\delta \tilde{q})^2 \rangle$.

III. EXPERIMENTAL CONDITIONS

The present data were obtained in the course of an earlier study (Ref. [15] or II). Although the basic decay characteristics of the velocity and temperature fields were presented in II, no attempt was made to check whether the statistics of θ at different x satisfied similarity. The time series obtained for II have been used to generate the structure functions which appear in Eqs. (4) and (6). Also, basic parameters which describe the decay of various quantities, e.g., $\langle q^2 \rangle$, $\langle \theta^2 \rangle$, $\langle \epsilon \rangle$, $\langle \chi \rangle$ were recalculated using a procedure analogous to that followed in I.

Velocity and temperature measurements were carried out at a mean velocity $U \simeq 6.4$ m/s downstream of a biplane grid-heated mandoline combination (a configuration similar to that of Warhaft and Lumley [2] and Sreenivasan *et al.* 1980 [3]). The grid was located at the entrance of the working section (350 mm×350 mm×2.4 m long) and was constructed of square bars (4.76 mm×4.76 mm). The mesh size M was 4.76 mm and the solidity was 0.35. The Reynolds number R_M was 10 564. The mandoline (mesh size $M_\theta = M$) was located at a distance of $1.5M$ downstream of the grid and comprised 5-mm-diameter chromel-A wires. For heating details, the reader should refer to II. The mean temperature increase, relative to ambient, was sufficiently small ($\simeq 2$ °C) for temperature to be considered passive. The probe (a sketch is shown in Fig. 1) consists of six wires, four (hot) operating in a constant-temperature mode (overheat ratio 1.5) and two (cold) operating in a constant current (0.1 mA) mode for measuring θ at two spatial locations. The four hot wires (one X wire+parallel hot wires) are arranged in order to measure one (lateral) vorticity component. When the X wire is in the (x,y) plane, u,v, and ω_z were obtained. Rotation through 90° yields u,w and ω_y (ω_y, and ω_z are the vorticity fluctuations on the y and z directions, respectively). The spatial resolution of this probe was discussed in Zhou and Antonia [16].

All wires were etched from Wollaston (Pt-10% Rh) to an active length of about $200 d_w$ for the hot wires ($d_w = 2.5$ μm) and $1000 d_w$ for the cold wires ($d_w = 0.63$ μm). The output signals from the constant temperature and constant current circuits were digitized (12-bit analog-to-digital converter) at a sampling frequency close to $2f_K$ (where $f_K \equiv U/2\pi\eta$ is the Kolmogorov frequency) after the low-pass filter cutoff frequency was set to be approximately equal to f_K. The digital records had a duration of about 55 s. Time series of α ($\equiv u, v, w, \theta$) were used to construct the temporal increment $\delta\alpha \equiv \alpha(t+\tau) - \alpha(t)$. Taylor's hypothesis was then invoked to interpret $\delta\alpha$ as a spatial increment. Present estimates of $\langle \epsilon \rangle$ and $\langle \chi \rangle$ were inferred from

$$\langle \epsilon \rangle = -\frac{U}{2} \frac{d\langle q^2 \rangle}{dx} \tag{34}$$

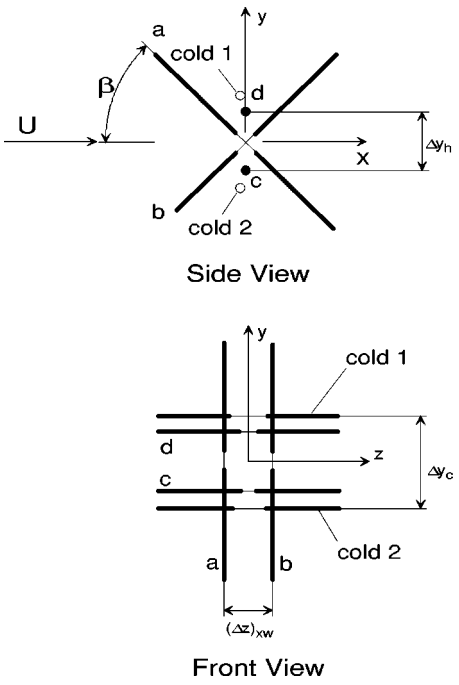

FIG. 1. Schematic arrangement of probe. *a* and *b* are inclined hot wires (X formation, separation $\Delta z_{xw} \simeq 1.5$ mm); *c* and *d* are parallel hot wires (separation $\Delta y_h \simeq 1.5$ mm); the parallel cold wires 1 and 2 are located about 0.3 mm upstream of *c* and *d*. Etched and unetched portions of the wires are shown by light and heavy lines, respectively. $\beta \simeq 50°$.

and Eq. (11), and were close ($\pm 10\%$) to those estimated (II) from the isotropic values of $\langle \epsilon \rangle$ and $\langle \chi \rangle$. The divergence (or longitudinal turbulent diffusion) terms, which were ignored in Eqs. (34) and (11), were two to three orders of magnitude smaller than the streamwise decay terms.

IV. COMPARISON BETWEEN EXPERIMENTAL RESULTS AND SIMILARITY REQUIREMENTS

In II, isotropic definitions for λ, R_λ, λ_θ, and Pe were used, based on isotropic values of $\langle \epsilon \rangle$ and $\langle \chi \rangle$. Here, we have preferred to use estimates of $\langle \epsilon \rangle$ and $\langle \chi \rangle$ inferred from Eqs. (34) and (11), and nonisotropic definitions of λ, λ_θ, R_λ, and Pe, as given in Sec. II.

In II, the effective origins and the exponents *m* and *n* were estimated using a trial and error method adopted by Comte-Bellot and Corrsin [17]. Different values of x_0 were selected and least-squares linear regressions were applied to $\ln\langle q^2 \rangle$ (or $\ln\langle \theta^2 \rangle$) vs $\ln(x - x_0)$. The optimum value for x_0 (estimated to be between *M* and $2M$) yielded the minimum deviation in *m* (or *n*). Here, we follow the procedure used in I, which focused on the behavior of λ^2. Accordingly, different choices of x_0 were applied and the ratios $\lambda^2/(x - x_0)$ and $\lambda_\theta^2/(x - x_0)$ were plotted (Fig. 2).

The optimum x_0 was that which produced the widest plateau. In both Figs. 2(a) and 2(b), $x_0 = 0$ appears to be the optimum choice (within $\pm 0.5M$) over the range $30 \leqslant (x - x_0)/M \leqslant 80$ and the values corresponding to the plateaus, when used in conjunction with Eqs. (21) and (20), yielded

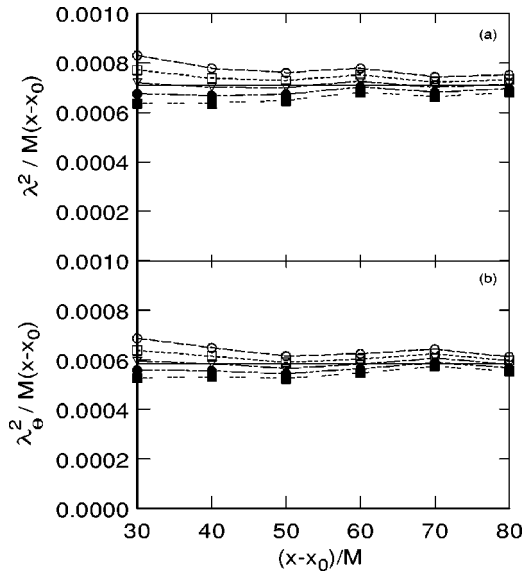

FIG. 2. Ratio of either λ^2 or λ_θ^2 with $(x - x_0)/M$ for different choices of x_0/M. (a) $(\lambda/M)^2/(x - x_0)/M$; (b) $(\lambda_\theta/M)^2/(x - x_0)/M$. The horizontal line in (a) yields $m = -1.33$; the horizontal line in (b) yields $n = -1.37$. ○, $x_0/M = 4$; □, 2; ▽, 0; ●, −2; ■, −4.

$m = -1.33$ and $n = -1.37$. These latter values agree almost exactly with those reported in II. This is perhaps not surprising since λ^2 and λ_θ^2 represent the ratios $\langle q^2 \rangle / \langle \epsilon \rangle$ and $\langle \theta^2 \rangle / \langle \chi \rangle$ and $\langle \epsilon \rangle$ and $\langle \chi \rangle$ are intimately related to $\langle q^2 \rangle$ and $\langle \theta^2 \rangle$ via Eqs. (11) and (34). The agreement reflects the internal consistency of the present data, and the (better than 10%) agreement between direct estimates of $\langle \epsilon \rangle$ and $\langle \chi \rangle$ from the probe and those inferred from Eqs. (34) and (11). The adequacy of the present estimates of *m* and *n* is further confirmed in Figs. 3 and 4. Over the range $30 \leqslant x/M \leqslant 80$, $\langle q^2 \rangle^{1/m}$ and $\langle \theta^2 \rangle^{1/n}$ increase linearly with *x* (Fig. 3) to a close approximation (the straight lines through the origin are least-squares linear regressions to the data). Similarly, good linear variations are exhibited in Fig. 4 by $\langle \epsilon \rangle^{1/(m-1)}$ and $\langle \chi \rangle^{1/(n-1)}$.

It follows from Eqs. (20) and (21) that

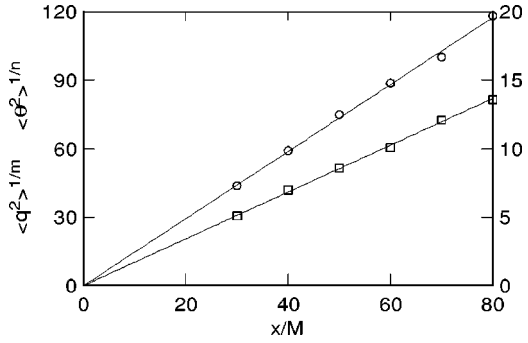

FIG. 3. Variations of $\langle q^2 \rangle^{1/m}$ (right vertical axis) and $\langle \theta^2 \rangle^{1/n}$ (left vertical axis) with x/M using the values of *m* and *n* estimated from Fig. 2. ○, $\langle \theta^2 \rangle^{1/n}$ $(n = -1.37)$; □, $\langle q^2 \rangle^{1/m}$ $(m = -1.33)$. The straight lines through the origin are least-squares regressions to the data.

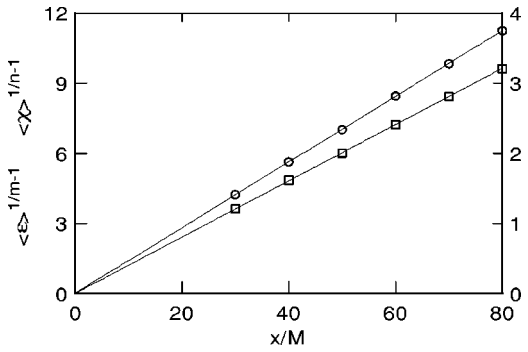

FIG. 4. Streamwise variation of $\langle\epsilon\rangle^{1/(m-1)}$ (right vertical axis) and $\langle\chi\rangle^{1/(n-1)}$ (left vertical axis) using the values of m and n estimated from Fig. 2. ○, $\langle\chi\rangle^{1/(n-1)}$ ($n=-1.37$); □, $\langle\epsilon\rangle^{1/(m-1)}$ ($m=-1.33$). $\langle\epsilon\rangle$ is in m^2/s^3 and $\langle\chi\rangle$ is in $°C^2/s$. The straight lines through the origin are least-squares regressions to the data.

$$\frac{\lambda_\theta^2}{\lambda^2}=\frac{3\kappa}{5\nu}\frac{m}{n}=\frac{3}{5}\mathrm{Pr}^{-1}R. \tag{35}$$

This ratio remains constant with x (Fig. 5) since R ($\equiv m/n$) is constant. Since $m<-1$, R_λ and Pe must decay with a power-law exponent given by $(m+1)/2$, in this case -0.16.

Distributions of f $[\equiv\langle(\delta\tilde{q})^2\rangle\equiv\langle(\delta q)^2\rangle/\langle q^2\rangle]$ and f_θ $[\equiv\langle(\delta\tilde{\theta})^2\rangle=\langle(\delta\theta)^2\rangle/\langle\theta^2\rangle]$ are shown in Fig. 6. In each case, the collapse is good over practically the complete range of $\tilde{r}$ or $\tilde{r}_\theta$. Note that f and f_θ have significantly different shapes, despite having the same limiting values as $\tilde{r}\to 0$ and $\tilde{r}\to\infty$. The quality of collapse for $f\equiv\langle(\delta\tilde{q})^2\rangle$ in Fig. 6 is comparable to that observed for a grid constructed from circular rods (M and the solidity being the same). To avoid crowding, distributions at only one value of x/M are shown in Fig. 7. The overshoot exhibited by f at $\tilde{r}\simeq 20$ for the circular rod grid is absent in the flow generated by a grid of square bars; here, the asymptotic value of 2 for f is approached monotonically. The overshoot implies some sort of large-scale organization; indeed, flow visualizations indicated that, for the grid constructed from circular rods, the initial strong periodicity associated with vortex shedding remained evident up to relatively large values of x/M. In the present flow, the initial periodicity is rapidly obliterated.

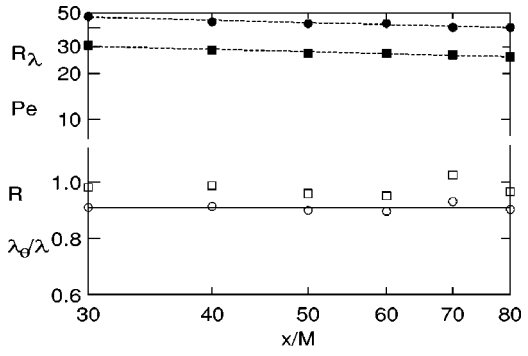

FIG. 5. Ratio λ_θ/λ between the Corrsin and Taylor microscales. The streamwise variations of R_λ and Pe are also shown. ○, λ_θ/λ;—, λ_θ/λ from Eq. (35), with $R=0.978$. □, R; ●, R_λ; ■, Pe. The broken lines are least-squares regressions to the R_λ and Pe data, each with a slope of -0.16 or $(m+1)/2$.

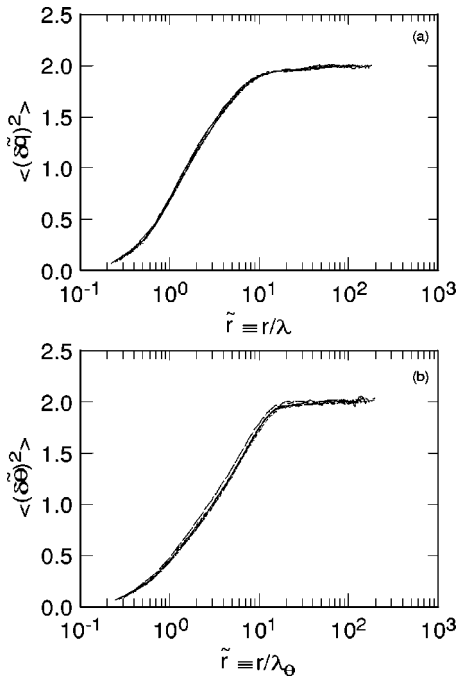

FIG. 6. Distributions of (a) $f\equiv\langle(\delta\tilde{q})^2\rangle=\langle(\delta q)^2\rangle/\langle q^2\rangle$ vs $\tilde{r}=r/\lambda$ and (b) $f_\theta\equiv\langle(\delta\tilde{\theta})^2\rangle=\langle(\delta\theta)^2\rangle/\langle\theta^2\rangle$ vs $\tilde{r}_\theta=r/\lambda_\theta$. – –, $x/M=30$; - - -, 40; — - —, 50; — - - —, 60; - - - – – –,70;– – – – – –,80.

Use of the Kolmogorov−Obukhov−Corrsin scales $U_K\equiv(\nu\langle\epsilon\rangle)^{1/4}$, $\theta_K\equiv(\langle\chi\rangle\eta/UK)^{1/2}$, and η for normalizing $\langle(\delta q)^2\rangle$, $\langle(\delta\theta)^2\rangle$, and r results in a good collapse only at small r^* (Fig. 8). In general, the asterisk will denote normalization by U_K, θ_K, and/or η. As x/M increases, the distributions peel off at smaller r^* and the plateaux occur at smaller $\langle(\delta q^*)^2\rangle$or $\langle(\delta\theta^*)^2\rangle$. This trend is expected since, in the limit $r^*\to\infty$,

$$\langle(\delta q^*)2\rangle=\frac{6}{15^{1/2}}R_\lambda$$

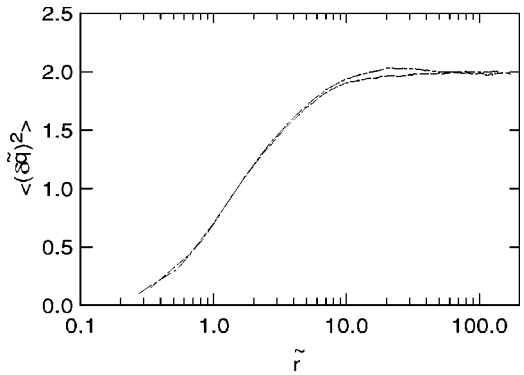

FIG. 7. Distributions of $\langle(\delta\tilde{q})^2\rangle$for two different grids. The mesh size M is the same for both grids. – –, present grid (square bars, $x/M=80$); — – —, grid used in I (circular rods, $x/M=80$).

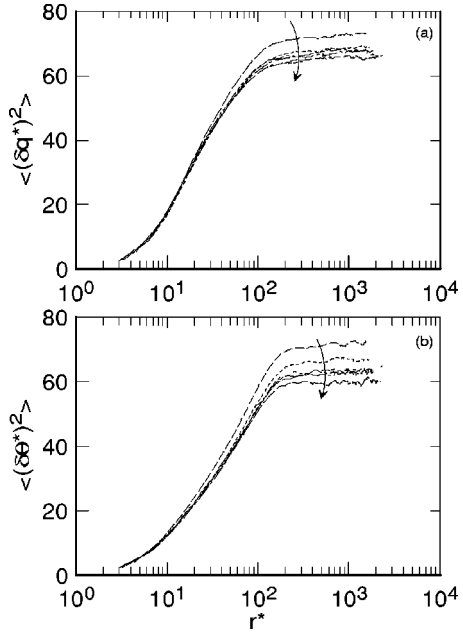

FIG. 8. Distributions of $\langle(\delta q)^2\rangle$and $\langle(\delta\theta)^2\rangle$ normalized using U_K, θ_K, and η. (a) $\langle(\delta q^*)^2\rangle$; (b) $\langle(\delta\theta^*)^2\rangle$. Line types as in Fig. 6. The curved arrows are in the direction of increasing x/M.

and

$$\langle(\delta\theta^*)2\rangle = \frac{6}{15^{1/2}} R_\lambda .$$

The trend at large r^* in Fig. 8 reflects the decrease of these two quantities as x/M increases (i.e., as R_λ decreases).

It was already noted that structure functions are more sensitive than spectra for testing departures from similarity because of the different nature (local vs integral) of the constraints that each need to satisfy. For example, whereas $\langle(\delta q^*)^2\rangle \to 2\langle q^{*2}\rangle$as $r^* \to \infty$ [Fig. 8(a)], it is the integral of the Kolmogorov-normalized spectrum ϕ_q^* which is equal to $\langle q^{*2}\rangle$. Spectra of q and θ are shown in Figs. 9 and 10, respectively, for the two types of normalization used in Figs. 6 and 8. Note that $\int_0^\infty \tilde{\phi}_q(\tilde{k}_1)d\tilde{k}_1 = 1$ and $\int_0^\infty \tilde{\phi}_\theta(\tilde{k}_1)d\tilde{k}_1 = 1$ whereas $\int_0^\infty \phi_q^*(k_1^*)dk_1^* = \langle q^{*2}\rangle$and $\int_0^\infty \phi_\theta^*(k_1^*)dk_1^* = \langle\theta^{*2}\rangle$. The product $k_1\phi_\alpha(k1)$ is plotted against $\ln k_1$ so that the areas under the distributions comply with the previous integral values. Although the spectral differences between the present similarity and a scaling based on Kolmogorov variables are more ambiguous than those inferred by comparing structure functions (Fig. 6 vs Fig. 8), the low wave number collapse based on $\lambda - \lambda_\theta$ [Figs. 9(a) and 10(a)] represents a small improvement relative to that when the normalization is on U_K, θ_K, and η [Figs. 9(b) and 10(b)].

The different shapes of the q and θ spectra reflect the previously noted differences between f and f_θ. The normalized distributions in Fig. 10 peak at a significantly smaller value of k_1 than the corresponding distributions in Fig. 9. A qualitatively similar difference between $\phi_q(k_1)$ and $\phi_\theta(k_1)$ has been observed in direct numerical simulations of decaying homogeneous isotropic turbulence in a periodic box

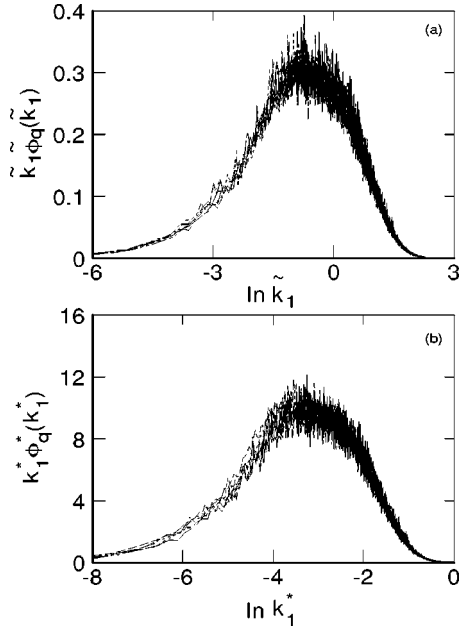

FIG. 9. Turbulent energy spectra multiplied by k_1 and plotted against $\ln k_1$. In (a), the normalization is by λ and $\langle q^2\rangle$. In (b), the normalization is by U_K and η. – –, $x/M = 30$; - - -, 40; — - —, 50; — - - —, 60; - - - - - -, 70; — —, 80.

([27]) for which nominally identical spectral shapes were assumed for the velocity and scalar fields at $t=0$. Another difference between ϕ_q and ϕ_θ is the appearance of a power-law scaling range in ϕ_θ, despite the small value of R_λ. No scaling range can be observed in ϕ_q. Figure 11 compares a smoothed distribution of $\tilde{\phi}_\theta(\tilde{k}_1)$ [to avoid the ambiguity due to the noise spikes of Fig. 10, a high-order polynomial was

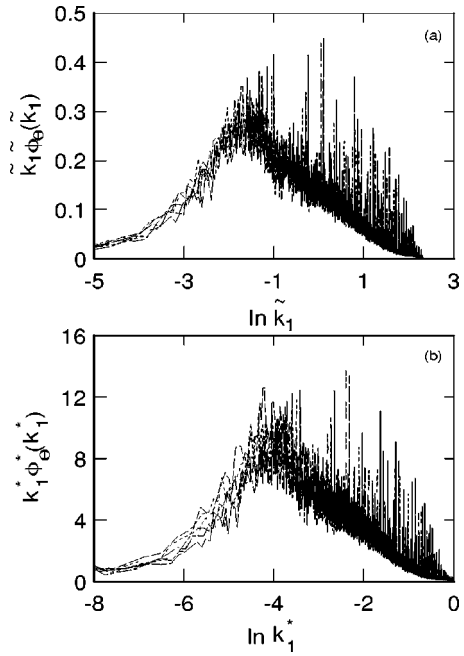

FIG. 10. Temperature spectra multiplied by k_1 and plotted against $\ln k_1$. In (a) the normalization is by λ_θ and $\langle\theta^2\rangle$. In (b), the normalization is by U_K, θ_K, and η. Symbols are as in Fig. 9.

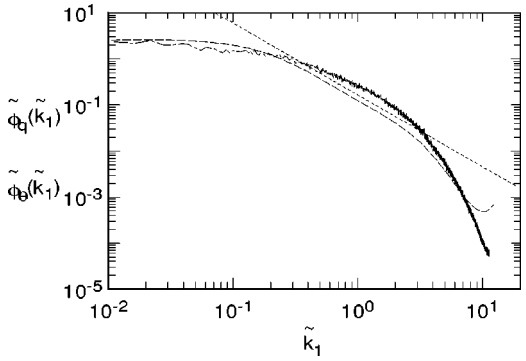

FIG. 11. Comparison between spectra of q and θ at $x/M=50$. The normalization uses $\langle q^2\rangle$, $\langle\theta^2\rangle$, λ, and λ_θ. —, $\tilde{\phi}_q(\tilde{k}_1)$; — - —, $\tilde{\phi}_\theta(\tilde{k}_1)$. The dashed line has a slope of -1.56.

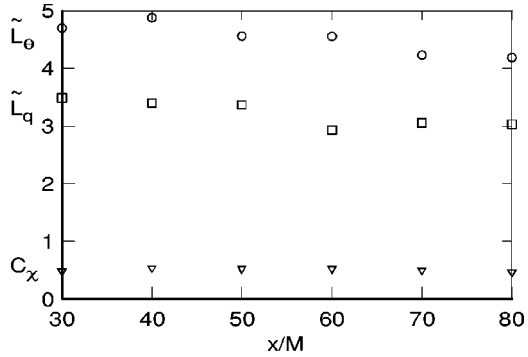

FIG. 12. Dependence of L_q/λ and L_θ/λ_θ on x/M. The variation of the coefficient C_χ is also shown. L_q and L_θ were obtained by integrating the autocorrelations inferred from Eq. (36). □, $\tilde{L}_q$; ○, $\tilde{L}_\theta$; ▽, C_χ, see Eq. (28).

first fitted to $\ln\phi_\theta(k_1)$] with an unsmoothed distribution of $\tilde{\phi}_q(\tilde{k}_1)$ on a log-log plot. A $\tilde{k}_1^{-1.56}$ power-law behavior can be observed over a surprisingly large range of $\tilde{k}_1$. This observation is consistent with that reported and discussed in detail by Jayesh *et al.* [18]. These authors found a scaling range, with an average exponent of -1.58, both when the temperature is introduced at (or near) the grid without a gradient and when a mean temperature gradient is introduced upstream of the grid. They also noted that the range dilates as the Reynolds number increases. Sreenivasan [19] commented that this anomalous behavior of the scalar spectrum in grid turbulence allowed an estimation of the Obukhov-Corrsin constant, even at modest Reynolds numbers. He also discussed the different behavior of the scalar spectrum in shear flows. Indeed, the present dissimilarity between $\tilde{\phi}_\theta(\tilde{k}_1)$ and $\tilde{\phi}_q(\tilde{k}_1)$ contrasts strongly with the close similarity that exists in shear flows (Chap. 7 of Chassaing *et al.* [20] reviews evidence for the spectral analogy between q and θ).

We did not try to calculate the integral length scales L and L_θ from the 3D spectra $E(k)$ and $E_\theta(k)$ since inferring these from the 1D spectra requires isotropy to be valid at all wave numbers. This is an inadequate assumption for the present flow at small wave numbers. Here, we have inferred the integral scales from the structure functions since ($\alpha\equiv q$ or θ)

$$\langle\tilde{\alpha}(x)\tilde{\alpha}(x+r)\rangle=1-\frac{\langle(\delta\tilde{\alpha})^2\rangle}{2}. \tag{36}$$

For $\alpha\equiv q$, the normalized correlation $\langle\tilde{q}(x)\tilde{q}(x+r)\rangle$ is identified with the sum $\langle\tilde{u}(x)\tilde{u}(x+r)\rangle+\langle\tilde{v}(x)\tilde{v}(x+r)\rangle+\langle\tilde{w}(x)\tilde{w}(x+r)\rangle$. The ratios L_q/λ and L_θ/λ_θ, where $L_\alpha=\int_0^{r_\alpha}\langle\tilde{\alpha}(x)\tilde{\alpha}(x+r)\rangle dr$ (r_α corresponds to the first zero crossing of the correlation), are shown in Fig. 12. Although there is some scatter in the data, the overall trend indicates that both ratios decrease slowly with x (by about 10% in the case of L_θ/λ_θ for $30\leqslant x/M\leqslant 80$), which is consistent with what was reported in I and the slower than $x^{1/2}$ growth rate for L_α. As discussed in I, it is possible that this result reflects the presence of the boundaries in the experiment. It is also axiomatic that the collapse of f and f_θ in Fig. 6 cannot be perfect since only a perfect collapse would be consist with $\tilde{L}_\alpha=$ constant. The estimation of L_χ, Eq. (28), requires C_χ to be known. If L_χ is identified with L_θ, C_χ can be obtained indirectly from Eq. (28). Its variation with x/M is included in Fig. 12. The average value appears to be constant ($\simeq$0.5), suggesting that the variation of $\tilde{L}_\theta$ with x/M reflects that of the Péclet number, Eq. (28).

The normalized third-order structure functions g and g_θ are shown in Figs. 13 and 14, respectively. The collapse for g (Fig. 13) is an improvement over that exhibited by Fig. 10(a) in I. This, together with the distributions of f [Fig. 6(a)] or $\tilde{\phi}_q(\tilde{k}_1)$ [Fig. 9(a)], reinforces the claim that the velocity field satisfies similarity to a good approximation. The calculation of g (Fig. 13), based on the measured distribution of f at $x/M=40$, approximately follows the measured distribution of g at $x/M=40$ up to $\tilde{r}\simeq 5$. The trend in Fig. 14 suggests that similarity of the temperature field may only be achieved at much larger values of x/M than for the velocity field. The distributions of g_θ at $x/M=70$ and $x/M=80$ are in excellent agreement with each other. The calculation of g_θ, based on the measured distribution of f_θ at $x/M=70$, follows the measured distribution of g_θ (also at $x/M=70$) quite closely up to $\tilde{r}_\theta\simeq 12$. It is not clear why this latter limit is greater than that in Fig. 13, but one would expect that the assumption of isotropy becomes more tenuous as $\tilde{r}$ (or $\tilde{r}_\theta$) increases. The level of agreement between measurement and

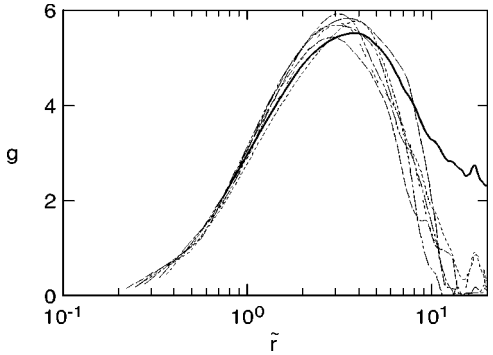

FIG. 13. Distributions of $g\equiv-3^{1/2}R_\lambda\langle(\delta\tilde{u})(\delta\tilde{q})^2\rangle$ vs $\tilde{r}\equiv r/\lambda$. Line types as in Fig. 6. The heavy solid line is a calculation based on Eq. (33) and the distribution of f at $x/M=40$.

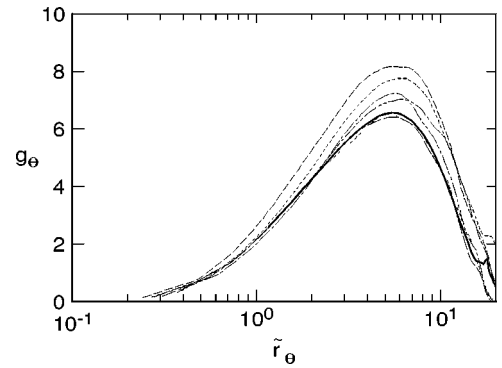

FIG. 14. Distributions of $g_\theta \equiv -3^{1/2}$ Pe $\langle(\delta\tilde{u})(\delta\tilde{\theta})^2\rangle$ vs $\tilde{r}_\theta \equiv r/\lambda_\theta$. Line types are as in Fig. 6. The heavy solid line is a calculation based on Eq. (26) and the measured distribution of f_θ at $x/M=70$.

calculation in Figs. 13 and 14 represents a significant improvement over that reported by Mills *et al.* [21] for triple velocity and velocity-temperature correlations. Details of the calculation were not given by these authors, but it is reasonable to assume that they were also based on a $\lambda-\lambda_\theta$ similarity of the correlation functions.

Finally, it is pertinent to comment on the expectation, which follows from Eqs. (31) and (32), that the products SR_λ and $S_\theta R_\lambda$ should remain constant (Sec. II) for fixed initial conditions. These equations automatically satisfy similarity if the equations from which they are derived, i.e., the equations for $\langle(\delta u)^2\rangle$ or $\langle(\delta\theta)^2\rangle$, satisfy similarity. From an experimental viewpoint, accurate testing of Eqs. (31) and (32), which weight small-scale structures, is delicate due mainly to spatiotemporal resolution and noise limitations of the measurements. For the present experiment, we have found that S and S_θ, as estimated from the limiting values of $\langle(\delta u)^3\rangle$ and $\langle(\delta u)(\delta\theta)^2\rangle$ as $r\to 0$, are approximately constant with respect to x. The average value of S is about 0.49 whereas that of S_θ is about 0.38. Since R_λ decreases with x, G and G_θ must therefore also decrease with x according to Eqs. (31) and (32). Our best estimates for G and G_θ were obtained by extrapolating the spectra of u and θ (Fig. 15) to large k_1 after ignoring the noise-contaminated portion of the spectrum. The values of G and G_θ (Fig. 16) decrease with x at approximately the same rate as R_λ or as the products (also included

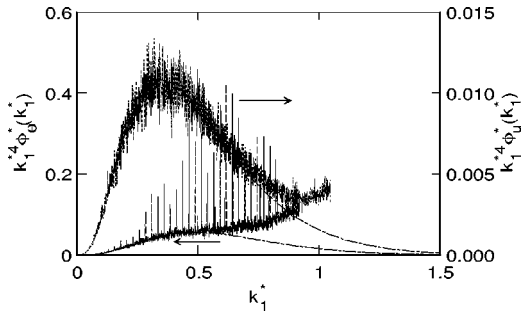

FIG. 15. Measured and smoothed extrapolated distributions of $k_1^{*4}\phi_u^*(k_1^*)$ and $k_1^{*4}\phi_\theta^*(k_1^*)$ at $x/M=50$. Solid curves, measured; dashed curves, smoothed and extrapolated.

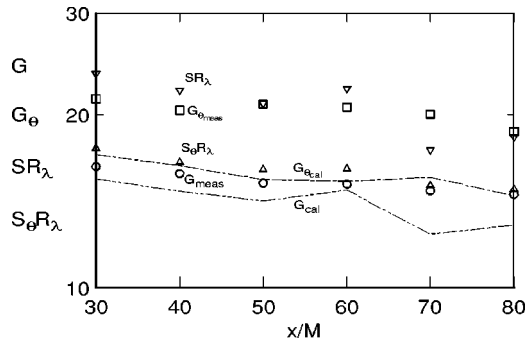

FIG. 16. Streamwise variations of G and G_θ. Also shown are the products SR_λ and $S_\theta R_\lambda$. ○, G_{meas}, measured G; — - - —, G_{cal}, G calculated using Eq. (31); □, $G_{\theta_{meas}}$, measured G_θ; — - —,$G_{\theta_{cal}}$, G_θ calculated using Eq. (32); ▽, SR_λ; △, $S_\theta R_\lambda$.

in the figure) SR_λ and $S_\theta R_\lambda$. Although the uncertainty (Fig. 15) in extrapolating the spectra is sufficiently large to prohibit any conclusion regarding the precise streamwise variations of G and G_θ, the trend with x/M in Fig. 16 is consistent with Eqs. (31) and (32). Calculations of G and G_θ, based on Eqs. (31) and (32) and measured values of S, S_θ, R_λ, are also shown in Fig. (16). The calculation underestimates G_{meas} by about 10% and $G_{\theta_{meas}}$ by about 27%. The discrepancy is most likely due to the systematic error in extrapolating G and more especially G_θ (Fig. 15). It can be claimed, nonetheless, that the streamwise decay of G and G_θ is consistent with our earlier observation that the collapse of f, f_θ, $\tilde{\phi}_q(\tilde{k}_1)$, and $\tilde{\phi}_\theta(\tilde{k}_1)$ is not perfect. The nonbalance of Eqs. (31) and (32), which are a very refined test of the small-scale behavior of Eqs. (5) and (6), simply emphasizes the fact that equilibrium similarity, as it was defined in Sec. II, is not respected for the very small scales.

The decay with x of the present SR_λ data contrasts with the apparent constancy for this product, as obtained in earlier grid turbulence experiments (see Fig. 10 of George [7]) but is consistent with the trend of the DNS results [22]. Recent DNS data (Antonia and Orlandi, [23]) for decaying homogeneous isotropic turbulence indicate that S and S_θ (it is understood here that temporal definitions apply for these two quantities) are approximately constant over a period of time for which $\langle q^2\rangle$ and $\langle\theta^2\rangle$ exhibit approximate power-law behaviors. The temporal decay of the products SR_λ and $S_\theta R_\lambda$ is consistent with the streamwise decay observed in the present experiment.

V. CONCLUDING DISCUSSION

All the terms in the transport equation of $\langle(\delta\theta)^2\rangle$ for decaying homogeneous isotropic turbulence remain in relative balance throughout the decay when the characteristic scale $\langle\theta^2\rangle$ for the scalar decays as x^n and the characteristic length scale grows as $x^{1/2}$. The microscales λ and λ_θ satisfy this latter requirement provided $\langle q^2\rangle\sim x^m$ and $\langle\theta^2\rangle\sim x^n$. As in the spectral analysis of Ref. [9], the present similarity solution should be valid regardless of the magnitude of the turbulent Reynolds and Péclet numbers. Both numbers can vary with x according to $x^{(m+1)/2}$, when $m<-1$. In the spe-

cial case, when m is equal to -1, R_λ and Pe remain constant and the present solution becomes consistent with the asymptotic result obtained in Ref. [10] which extended the analysis of Ref. [8]. The dissipation time scale ratio R must be constant with x irrespective of the values of m and n. The magnitude of this ratio will, like m and n, depend on the initial conditions.

Measurements, at small R_M (and therefore R_λ), downstream of a grid-mandoline combination satisfy the requirements of our analysis and those of Ref. [9] reasonably well. Although the assumption of homogeneous isotropic turbulence is approximated poorly by the large scales of the flow, the measured distributions of f, f_θ, collapse reasonably when plotted against r/λ or r/λ_θ. The collapse for the appropriately normalized third-order velocity structure function g is adequate as is the calculation of g based on the present similarity solution. The departure between measurement and calculation occurs at large r/λ and is reconcilable with the expected departure of the large scales from homogeneity and isotropy. Measurements of g_θ, the normalized mixed velocity-temperature structure function, exhibit poorer collapse than for g, possibly implying that larger values of x/M may be necessary for the scalar field to attain similarity.

Several further comments can be made with regard to the quality of similarity achieved in the experiment. First, it is clear that the collapse of f and f_θ, or indeed that of the corresponding spectra, is not perfect. If it were, then the integral length scales would be exactly proportional to λ or λ_θ. This is not the case since the integral scales grow more slowly than $x^{1/2}$, most likely reflecting the effect of the lateral boundaries of the working section of the wind tunnel. Second, our measurements indicate that different initial conditions lead to different similarity solutions. The distribution of f_θ is also expected to depend on initial conditions. The observed strong dissimilarity between the shapes of f and f_θ or between those of the energy and temperature spectra appears to be a peculiarity of decaying turbulence. The addition of a mean temperature gradient does not seem to affect this dissimilarity since the ''anomalous'' power-law scaling range that is observed in the temperature spectrum, but not in the energy spectrum, is also found when the grid interacts with a mean temperature gradient (Jayesh *et al.* [18]). The dissimilarity disappears when a relatively strong mean velocity gradient and a mean temperature gradient are present. In such a case, the shapes of the energy and temperature spectra are quite similar (e.g., Fulachier and Antonia [24]). Thirdly, the present calculations of g and g_θ represent an improvement over earlier attempts at reconciling calculations of third-order velocity or velocity-temperature correlation functions with measurements. In particular, as was noted in I in the context of g, calculations based on the Kolmogorov [25] or Yaglom [26] equations which ignore Γ_1, Γ_2, Γ_{θ_1}, and Γ_{θ_2} would only be adequate at very large values of R_λ and Pe.

The results presented here are consistent with those [for $E_\theta(k)$ and $T_\theta(k)$] obtained using DNS in Ref. [12]; in particular, George [9] provides a good means for calculating $\langle \delta u(\delta\theta)^2 \rangle$ or $T_\theta(k)$, but Kolmogorov/Corrsin scales are more appropriate in terms of collapsing the spectra at large wave numbers than George's variables.

While it is desirable to test similarity at higher values of R_M than in the present experiment, we expect that the experimental difficulties will only increase as R_M is increased. Also, the percentage streamwise variation of R_λ is expected to diminish as R_M is increased. As a suggestion for future work, a more fruitful way to proceed experimentally may be to improve the isotropy of the flow, for example by using a secondary contraction downstream of the grid as in Comte-Bellot and Corrsin (1966) [17], while making every effort to minimize the influence from the tunnel working section walls.

ACKNOWLEDGMENTS

R.A.A. acknowledges the support of the Australian Research Council and many useful discussions with W.K. George.

[1] S. Corrsin, J. Aeronaut. Sci. **18**, 417 (1951).
[2] Z. Warhaft and J.L. Lumley, J. Fluid Mech. **88**, 659 (1978).
[3] K.R. Sreenivasan, S. Tavoularis, R. Henry, and S. Corrsin, J. Fluid Mech. **100**, 597 (1980).
[4] T. Von Karman and L. Howarth, Proc. R. Soc. London, Ser. A **164**, 192 (1938).
[5] R.A. Antonia, R.J. Smalley, T. Zhou, F. Anselmet, and L. Danaila, J. Fluid Mech. **487**, 245 (2003).
[6] A. S. Monin and A. M. Yaglom, *Statistical Fluid Mechanics* (MIT Press, Cambridge, MA, 1975).
[7] W.K. George, Phys. Fluids A **4**, 1492 (1992).
[8] C.G. Speziale and P.S. Bernard, J. Fluid Mech. **241**, 645 (1992).
[9] W. K. George, in *Studies in Turbulence*, edited by T. B. Gatskii, S. Sarkar, and G. Speziale (Springer-Verlag, Berlin, 1992).
[10] M. Gonzalez and A. Fall, Phys. Fluids **10**, 654 (1998).
[11] G. Comte-Bellot and S. Corrsin, J. Fluid Mech. **48**, 273 (1971).
[12] R. A. Antonia and P. Orlandi, in *Turbulence, Heat and Mass Transfer 4*, edited by H. Hanjalik, Y. Nagano, and M. Tammers (Begell House, 2003), pp. 131–138.
[13] L. Danaila, F. Anselmet, T. Zhou, and R.A. Antonia, J. Fluid Mech. **391**, 359 (1999).
[14] G.K. Batchelor and A.A. Townsend, Proc. R. Soc. London, Ser. A **190**, 534 (1947).
[15] T. Zhou, L. Danaila, R.A. Antonia, and F. Anselmet, Exp. Fluids **28**, 143 (2000).
[16] T. Zhou and R.A. Antonia, Phys. Fluids **12**, 335 (2000).
[17] G. Comte-Bellot and S. Corrsin, J. Fluid Mech. **25**, 657 (1966).
[18] Jayesh C. Tong and Z. Warhaft, Phys. Fluids **6**, 306 (1994).
[19] K.R. Sreenivasan, Phys. Fluids **8**, 189 (1996).

[20] P. Chassaing, R. A. Antonia, F. Anselmet, L. Joly, and S. Sarkar, *Variable Density Fluid Turbulence* (Kluwer Academic, Dordrecht, 2002), pp. 167–200.
[21] R. R. Mills, A. L. Kistler, V. O'Brien, and S. Corrsin, NACA Technical Note 4288, 1958.
[22] W. K. George (private communication).
[23] R. A. Antonia and P. Orlandi, Appl. Mech. Rev. **56**, 615 (2003).
[24] L. Fulachier and R.A. Antonia, Int. J. Heat Mass Transfer **27**, 987 (1984).
[25] A.N. Kolmogorov, Proc. R. Soc. London, Ser. A **434**, 9 (1991).
[26] A.M. Yaglom, Dokl. Akad. Nauk SSSR **69**, 743 (1949).
[27] P. Orlandi (private communication).